scientific reports

Check for updates

OPEN

Flexible and printable thermoelectric films based on $FeCl_3$ doped P3HT

Vaishali Rathi[1]✉, Manoj Sathwane[2], Kamal Singh[3], K. P. S. Parmar[3], Pradip K. Maji[2], Ranjeet K. Brajpuriya[3]✉ & Ashish Kumar[3,4]✉

Conductive polymers possess several advantageous properties, including cost-effectiveness, non-toxicity, and low thermal conductivity, making them promising candidates for thermoelectric (TE) applications. In this study, flexible films of poly (3-hexylthiophene) (P3HT) doped with $FeCl_3$ were synthesized via the drop-casting method using $FeCl_3$ concentrations of 20, 40, and 60 mM. The structural, morphological, and thermoelectric properties of the doped P3HT films were systematically investigated. Characterization techniques such as XRD, FTIR, and Raman spectroscopy revealed significant microstructural changes upon doping. XRD analysis indicated a transition from a crystalline to a more amorphous structure, while FTIR and Raman spectroscopy confirmed the formation of localized states through shifts in vibrational modes. SEM and AFM analyses demonstrated substantial morphological changes with $FeCl_3$ doping, and XPS confirmed the successful incorporation of $FeCl_3$ into the P3HT matrix. Thermoelectric measurements showed a notable enhancement in electrical conductivity, increasing from 4.37×10^{-4} S/cm (undoped film) to 46.67 S/cm for the P40-doped film at room temperature. The P40 sample also exhibited a high Seebeck coefficient of 164 μV/K and achieved a maximum power factor of 127.4 μW/m·K^2. These results highlight the potential of $FeCl_3$ doping in enhancing thermoelectric performance. The freestanding flexible P3HT films displayed a significantly high p-type Seebeck coefficient, emphasizing their suitability for thermoelectric applications. Future work should aim at optimizing doping conditions and exploring the integration of these materials into practical thermoelectric devices.

Keywords Organic thermoelectric (OTE), P_3HT, $FeCl_3$, Inorganic salt, Anionic conduction

Thermoelectricity is an energy-harvesting technology that has gained considerable global attention due to its ability to convert waste heat into usable electrical energy. In recent years, there has been growing emphasis on the development of thermoelectric (TE) materials that are not only efficient at room temperature but also scalable, cost-effective, printable on flexible substrates, and environmentally benign[1,2]. Among various material classes, conducting polymers have emerged as a promising category for thermoelectric, photovoltaic, and energy storage applications. Their advantages include solution processability, mechanical flexibility, low thermal conductivity, and compatibility with low-cost fabrication techniques, making them ideal candidates for next-generation flexible electronics[3,4].

The performance of a thermoelectric material is quantified by the dimensionless figure of merit, ZT, expressed as:

$$\mathrm{ZT} = \frac{S^2\sigma}{\kappa}.\mathrm{T} \tag{1}$$

where T is the absolute temperature, κ is thermal conductivity, σ is electrical conductivity, and SS is the Seebeck coefficient. The term $S^2\sigma$ is known as the power factor (PF). From Eq. (1), it is evident that high thermoelectric

[1]Department of Chemistry, School of Advanced Engineering, UPES, Bidholi, Dehradun, India. [2]Department of Polymer and Process Engineering, Indian Institute of Technology Roorkee, Roorkee, India. [3]Department of Physics, School of Advanced Engineering, UPES, Bidholi, Dehradun, India. [4]Department of Physics and Astronomical Science, Central University of Jammu, Samba, Jammu, J&K, India. ✉email: vaishali25011996@gmail.com; ranjeetbjp1@gmail.com; dr.akmr@gmail.com

performance requires materials with a high power factor and low thermal conductivity to maintain a strong thermal gradient. However, these parameters—S, σ, and κ—are often interdependent, posing a challenge to their independent optimization[5].

Conducting polymers naturally exhibit low thermal conductivity and mechanical robustness, making them suitable for thermoelectric applications. By tuning charge carrier concentration and mobility, these materials offer potential for improved electrical performance. However, one limitation of conducting polymers is their relatively low Seebeck coefficient[6–8]. Recent studies suggest that incorporating ionic transport mechanisms can enhance the thermoelectric voltage in these materials[6,7,9]. For instance, PEDOT: PSS-PSSNa has demonstrated a high Seebeck coefficient, partly attributed to ionic contributions[7,8,10]. This behavior, associated with the Soret effect, arises from the thermodiffusion of ions under a thermal gradient[7,8,10–12]. Combining conducting polymers with polyelectrolytes has been shown to improve the overall power factor by leveraging both electronic and ionic contributions.

Poly(3-hexylthiophene) (P3HT) has garnered significant attention as a solution-processable organic semiconductor due to its ease of synthesis, good solubility in common organic solvents, and potential for high charge mobility arising from its semi-crystalline microstructure[13–15]. P3HT can be processed via various techniques such as drop casting, spin coating, dip coating, solution casting, and bar coating. Several efforts have been made to improve the TE performance of P3HT through chemical doping or blending with inorganic and organic nanomaterials[16–19]. For example, Zhu et al. utilized triflimide anions as dopants to enhance the power factor of P3HT[20], while Qiu et al. reported composite films of Bi_2Te_3 nanowires and P3HT with improved power factors of 13.6 $\mu W \cdot m^{-1} \cdot K^{-2}$ at 300 K[13]. Muller et al. achieved a significantly higher power factor of 95 ± 12 $\mu W \cdot m^{-1}$ K^{-2} at room temperature by doping $FeCl_3$ into P3HT/CNT composite films[16]. Despite these advancements, studies focused specifically on the thermoelectric behavior of doped P3HT films remain limited and warrant further exploration.

In this work, we report the incorporation of $FeCl_3$ as a dopant in P3HT films to enhance their thermoelectric properties. The doped films demonstrated a power factor exceeding 127.4 $\mu W \cdot m^{-1} \cdot K^{-2}$ at room temperature. A comprehensive analysis was performed to investigate the correlation between Seebeck coefficient, electrical conductivity, and temperature in these films. Their microstructural and compositional characteristics were examined using techniques such as XPS, XRD, SEM, and EDS, providing insights into the role of $FeCl_3$ doping in modulating the thermoelectric performance of P3HT.

Experimental procedure

Poly (3-hexylthiophene) (P3HT) with a molecular weight of 37,685 g/mol and regioregularity of 98.5%, along with anhydrous $FeCl_3$, was procured from Sigma-Aldrich (USA). The solvents, nitrobenzene and chloroform, were obtained from Alfa Aesar (USA). All chemicals were used as received, without any additional purification.

Fabrication of P3HT films

P3HT powder was dissolved in chloroform to prepare a homogeneous 20 mg/mL solution using magnetic stirring for two hours. The resulting solution was drop-cast onto polyimide substrates under ambient laboratory conditions (25 ± 2 °C temperature and 40–50% relative humidity), The films were allowed to air dry naturally, during which solvent evaporation occurred gradually over ~ 25–30 min. To ensure complete removal of residual solvent and uniform film formation, the samples were subsequently baked at 70 °C for 30 min in a hot-air oven.

$FeCl_3$ was dissolved in nitrobenzene at the required concentrations of (20, 40, and 60 mM) and stirred using a magnetic stirrer a for 1 h at room temp (~ 25 °C) to ensure complete dissolution and homogeneity of the solution. No external heating was applied during this process, as $FeCl_3$ readily dissolves in nitrobenzene at ambient conditions. Doping was carried out by immersing the dried P3HT films into the $FeCl_3$ solutions for two minutes. The doped samples were labeled as follows: P0 (undoped), P20 (20 mM $FeCl_3$), P40 (40 mM $FeCl_3$), and P60 (60 mM $FeCl_3$). Upon immersion, the pristine golden color of the films changed instantly to a shiny black, indicating successful doping. All film types (P0, P20, P40, and P60) were prepared in triplicate under identical conditions to assess reproducibility. For each batch, the $FeCl_3$ doping solutions were freshly prepared at the same concentrations, and the immersion time and environmental conditions were strictly controlled. Interestingly, all doped films detached cleanly from the substrate after drying, forming freestanding, flexible films. These conditions were kept identical for all films to maintain reproducibility. The controlled evaporation and mild heating step were crucial for obtaining smooth, crack-free films with consistent thickness (~ 12 µm). The film thickness was measured using a stylus profilometer (Bruker DektakXT) by recording the step height between the film and the substrate after scratching a small portion of the surface. Measurements were taken at three different regions for each sample, and the average thickness was found to be ~ 12 ± 0.5 µm across multiple batches, confirming reproducibility. This fabrication method is scalable and can be applied to both rigid (glass) and flexible (e.g., Kapton tape) substrates with customized specifications. Figure 1 illustrates the step-by-step process of film synthesis and shows photographs of the resulting undoped and doped freestanding films.

Film characterization

The structural, electronic, and thermoelectric properties of the prepared films were thoroughly characterized. Grazing incidence X-ray diffraction (GIXRD, Malvern Panalytical, USA) with Cu Kα radiation (λ = 1.54 Å) was employed to investigate the crystal structure. Raman spectroscopy, using a 532 nm green laser, was used to analyze conformational changes in the film structure. High-resolution morphological analysis was conducted using a field-emission scanning electron microscope (FESEM, Zeiss Gemini) and atomic force microscopy (AFM, NT-MDT INTEGRA) to study surface variations. All morphological measurements were performed at room temperature to ensure consistency. Fourier-transform infrared spectroscopy (FTIR, PerkinElmer) was

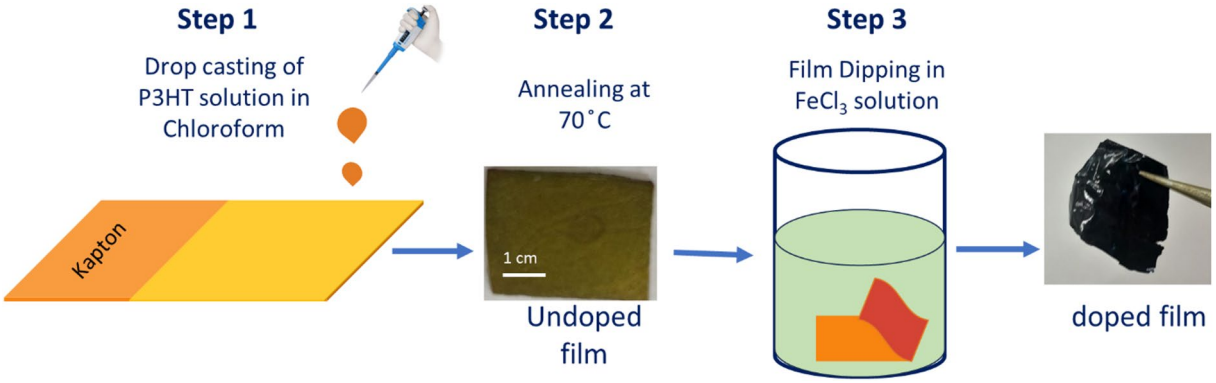

Fig. 1. An illustration of the P3HT film synthesis process for undoped and doped (freestanding) films.

used to detect changes in the chemical structure after doping. Thermoelectric measurements, including Seebeck coefficient and electrical resistivity, were carried out using an in-house developed setup as previously reported[21].

Result and discussion

Microstructural analysis (XRD, RAMAN)

For all characterizations, a consistent labeling scheme was used as follows:

Sample description	Label
Undoped P3HT film (0% $FeCl_3$)	P0
20 mM $FeCl_3$ in P3HT	P20
40 mM $FeCl_3$ in P3HT	P40
60 mM $FeCl_3$ in P3HT	P60

X-ray diffraction (XRD) spectra were recorded in the low-angle range (0°–30°) for all freshly prepared, freestanding thin-film samples, as shown in Fig. 2. The XRD pattern of the undoped P3HT film (P0) exhibited three distinct diffraction peaks at 2θ values of 5.3°, 10.7°, and 16.15°, corresponding to the (100), (200), and (300) crystallographic planes, respectively. These intense reflections are indicative of a predominantly crystalline structure, characterized by edge-on stacking of P3HT lamellae, as reported in earlier studies[22,23]. A minor hump at 27° suggests the presence of amorphous regions within the film. The well-ordered arrangement of polymer chains in P0 is attributed to π–π stacking between aromatic rings, resulting in a layered structure with an interchain spacing of approximately 0.167 nm—a configuration resembling a zipper-like packing of lateral alkyl side chains[20,23].

In contrast, the doped films (P20, P40, and P60) showed broader and less intense (100) peaks at lower 2θ values of 5.15°, 4.56°, and 4.42°, respectively, with corresponding full widths at half maximum (FWHM) of approximately 0.99, 0.87, and 0.97 showing in Table 1. The shift to lower angles reflects an increased out-of-plane stacking distance, likely due to ion intercalation between polymer chains, leading to the expansion of interplanar spacing[13,16,22–24].

Relative crystallinity was quantified by calculating the ratio of the area under the crystalline peak (primarily the (100) reflection) to the total area under the XRD curve. The undoped film (P0) displayed a crystallinity index of approximately 72%, which decreased significantly to 41%, 28%, and 19% for the P20, P40, and P60 samples, respectively. This reduction confirms the progressive loss of structural order and supports the amorphization trend inferred from the broadening and shift of the (100) peak.

Raman spectra of both undoped and doped films were collected in the 600–1600 cm^{-1} range, as presented in Fig. 3. For the undoped sample (P0), the most prominent peak appeared at 1440 cm^{-1}, corresponding to the Cα = Cβ stretching vibration. Upon doping, this band underwent a blue shift to 1444 cm^{-1}, indicating the formation of bipolarons and a reduction in molecular planarity induced by dopant–polymer interactions[25]. This shift is attributed to the stiffening of the vibrational mode within the bipolaron band, consistent with reduced conjugation and planarity. In addition, the Cβ–Cβ intra-ring stretching mode, originally located at 1374 cm^{-1} in the undoped sample, exhibited a red shift to 1368 cm^{-1} and noticeable broadening in the doped films. This trend suggests an increase in structural disorder and the presence of more amorphous regions, in agreement with the XRD data. The doped samples also showed inter-ring C–C stretching near 1203 cm^{-1} and C–S–C deformation bands around 719–721 cm^{-1}. The red shift and broadening of the C–S–C modes indicate deformation in the thiophene rings, likely resulting from tensile strain introduced by $FeCl_3$ doping. This strain promotes a more linear (quinoid-like) backbone conformation[23,25].

The quinoid configuration emerges due to linearization of the P3HT chains upon $FeCl_3$ intercalation. Similar vibrational signatures associated with quinoid formation have been previously reported by Yamamoto and Furukawa[25]. Notably, in the highly doped P60 sample, an additional strong peak appeared at 1501 cm^{-1}. This

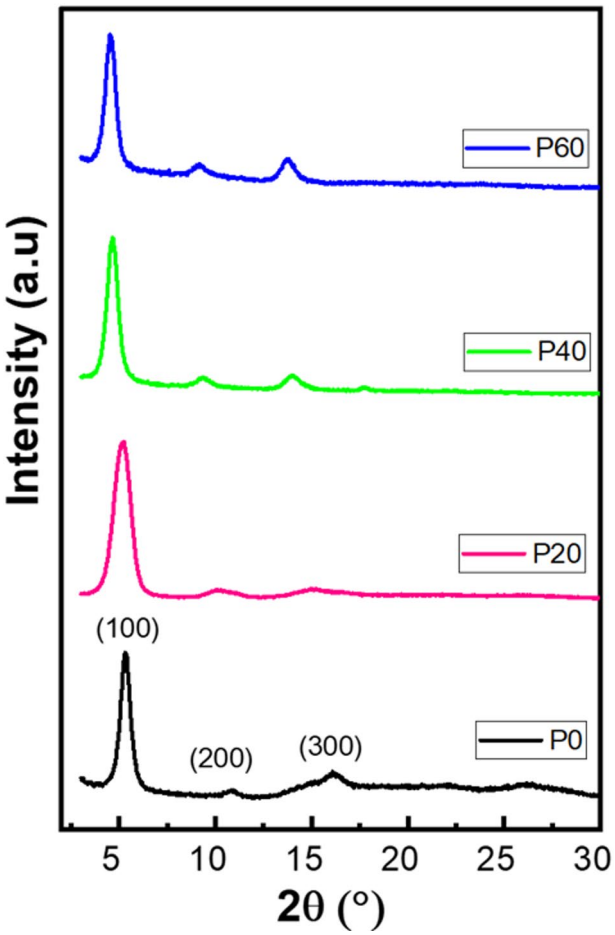

Fig. 2. X-ray diffraction patterns of undoped (P0) and $FeCl_3$-doped P3HT films (P20, P40, and P60).

Sample	2θ (°) (observed)	d-spacing (nm) (Bragg)	FWHM (°)	Crystallite size D (nm) (Scherrer)
P0 (undoped)	5.30	1.665	1.01	5.9
P20	5.15	1.714	0.99	8.0
P40	4.56	1.935	0.87	9.1
P60	4.42	1.997	0.97	8.2

Table 1. Comparative XRD parameters of undoped (P0) and $FeCl_3$-doped P3HT films (P20, P40, P60), showing the shift of the (100) diffraction peak, d-spacing, FWHM, and crystallite size, peak intensity.

vibrational mode, absent or negligible in the lower-doped films, is attributed to doping-induced vibrational activity linked to localized polaron and bipolaron species.

Collectively, these Raman spectral changes confirm the disruption of the P3HT microstructure, enhanced amorphization, and the formation of strain-induced linear (quinoid-type) conformations with increasing dopant concentration see the Fig. 4.

Surface morphology (FESEM and AFM)

The surface morphology of undoped and $FeCl_3$-doped P3HT films was investigated using Field-Emission Scanning Electron Microscopy (FESEM) and Atomic Force Microscopy (AFM), as illustrated in Figs. 5 and 6, respectively. FESEM images (Fig. 5) show that the undoped P3HT film (P0) possesses a relatively smoother surface compared to the doped films. The doped samples (P20, P40, and P60) exhibit a granular morphology, with particle sizes estimated at approximately 36 nm, 78 nm, and 92 nm, respectively, based on ImageJ analysis. While a general trend of increasing particle size with higher $FeCl_3$ concentration is observed, the change is neither strictly linear nor dramatically pronounced across the series. This suggests that although $FeCl_3$ promotes granular structure formation, its influence on particle growth saturates beyond a certain doping level. To further investigate elemental composition, Energy-Dispersive X-ray Spectroscopy (EDX) was conducted for the doped samples (Fig. 5e). The analysis confirmed the presence of key elements: carbon (C), oxygen (O), sulfur (S), iron

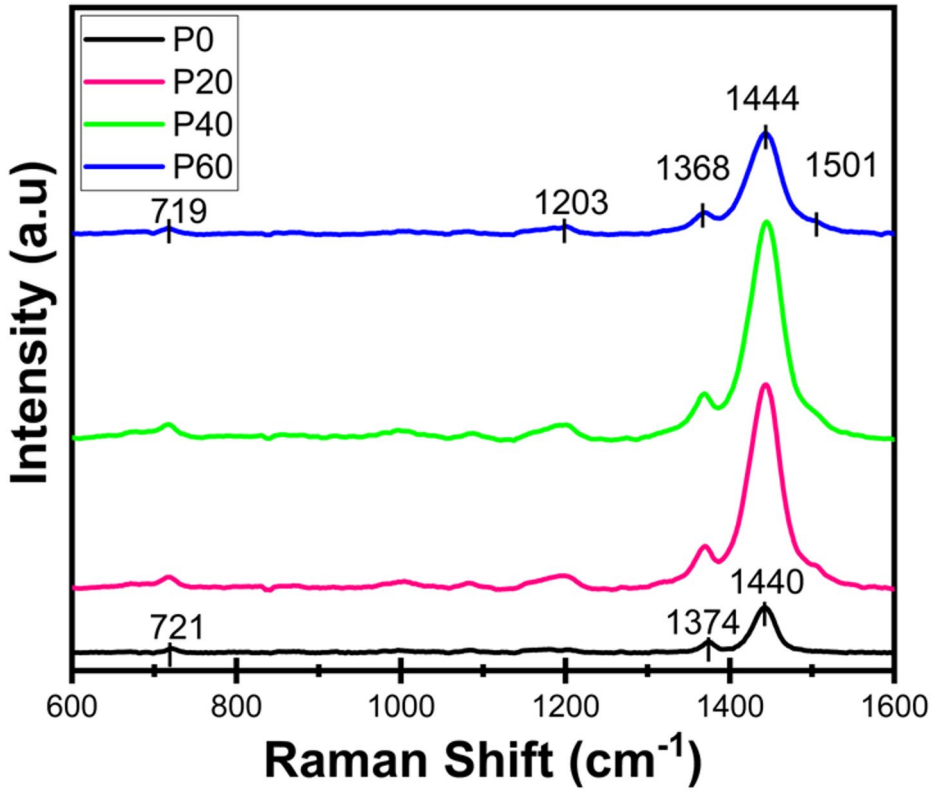

Fig. 3. Raman spectra of undoped (P0) and $FeCl_3$-doped P3HT films (P20, P40, and P60) showing vibrational mode shifts and intensity changes.

(Fe), and chlorine (Cl), consistent with the composition of the P3HT-$FeCl_3$ composite system. A quantitative summary of elemental distribution is presented in the inset of Fig. 5e. AFM imaging (Fig. 6) provided additional insight into the surface texture and roughness. The undoped sample (P0) exhibited a relatively smooth granular surface with a root mean square roughness (Rq) of ~ 42 nm over a 5 µm × 5 µm area. Upon doping with $FeCl_3$, surface roughness increased significantly, with Rq values measured at 84 nm (P20), 96.1 nm (P40), and 108 nm (P60). The increase in roughness correlates with the development of coarser surface features upon doping. Overall, both FESEM and AFM analyses confirm the formation of a progressively granular surface morphology with increased $FeCl_3$ doping. This evolution in surface topography may influence charge transport pathways and interfacial interactions, thereby affecting the thermoelectric behavior of the films.

Electronic structure (FTIR and XPS)

The FTIR spectra of undoped (P0) and $FeCl_3$-doped P3HT films (P20, P40, and P60) are shown in Fig. 7. The spectra reveal distinct differences in peak positions and intensities between undoped and doped samples.

In the undoped P3HT (P0), the characteristic in-plane C–H vibrational band appears at 1021 cm^{-1}, while the out-of-plane C–H bending vibrations are observed at 713 cm^{-1} and 820 cm^{-1}. A prominent peak at 1346 cm^{-1} is attributed to the deformation vibration of the $-CH_3$ group in the P3HT structure. In contrast, the doped samples exhibit a series of new absorption bands at 1384, 1282, 1142, 1089, 977, 854, and 820 cm^{-1}, which are commonly associated with polaronic states in chemically doped P3HT[25,26]. Among these, the band at 1142 cm^{-1} shows significantly higher intensity than those at 1384 and 1282 cm^{-1}. The strong 1142 cm^{-1} band is widely recognized as a signature of bipolaron formation, corresponding to symmetric C–C stretching vibrations associated with delocalized positive charges along the polymer backbone[27,28]. These observations suggest that bipolarons are the dominant charge carriers in the doped films. The FTIR results are further substantiated by X-ray Photoelectron Spectroscopy (XPS) analysis.

XPS measurements were carried out on selected samples—specifically, the undoped P0 film and the doped P40 film. The wide-scan XPS spectrum (Fig. 8a) of the undoped sample displays peaks corresponding to C1s, O1s, S2p, and Cl2p (the latter originating from residual chloroform). In the doped sample (P40), an additional Fe2p peak is observed, confirming the incorporation of iron from $FeCl_3$. The high-resolution C1s spectra of the undoped film (Fig. 8b) reveal two main components: one attributed to C–C/C–H bonding and the other to C–S bonds. The peak corresponding to C–S bonding appears at a slightly higher binding energy (285.1 eV), due to the electron-withdrawing effect of sulfur atoms. In the doped sample (Fig. 8c), the C1s peak shifts to 285.3 eV, indicating a higher concentration of carbon atoms in modified chemical environments. This shift is consistent with previous reports on higher doping levels[30]. The S2p spectrum of the undoped film (Fig. 8d) shows the typical spin-orbit splitting between $S2p_{3/2}$ and $S2p_{1/2}$, with a separation ΔBE of 1.6 eV—characteristic of sulfur–

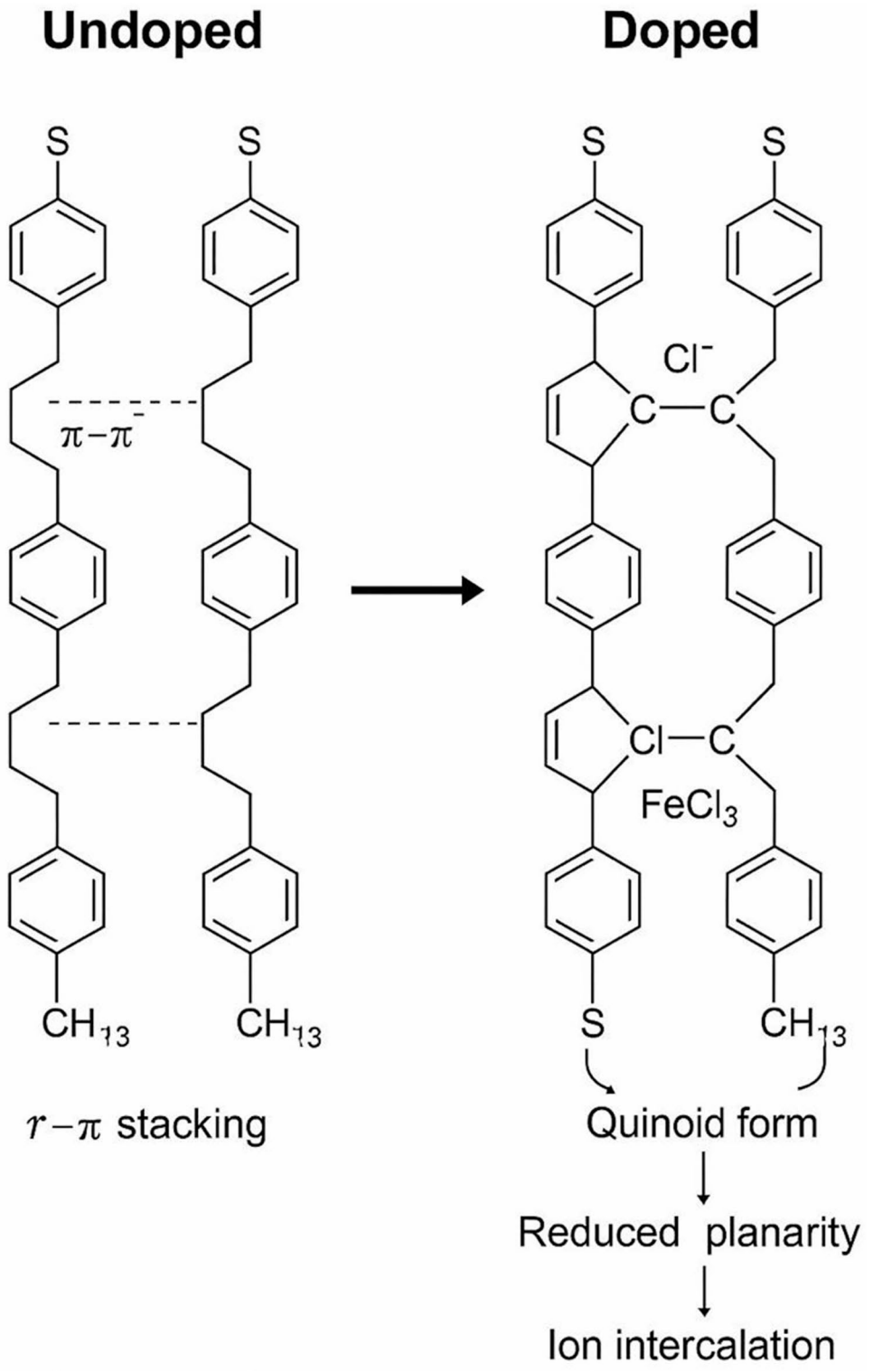

Fig. 4. Structural transformation of P3HT upon FeCl3 doping induces a quinoid structure, reduces planarity, and enables Cl- ion intercalation, disrupting Π-Π stacking.

carbon bonding in thiophene rings[31]. In the doped film (Fig. 8e), the $S2p_{3/2}$ peak shifts to 167 eV, indicating partial oxidation of the thiophene units due to $FeCl_3$ doping[29,32].

The Fe2p spectrum for the P40 film (Fig. 8g) shows two peaks for $Fe2p_{3/2}$ at 708.9 and 712.7 eV. These are associated with different oxidation states of Fe, consistent with the formation of Fe_2Cl_6 dimers that decompose into $Fe_2Cl_5^+$ and $Fe_2Cl_7^-$ species[34,35], as reported by Tosi et al.[33]. Additionally, the Cl2p region (Fig. 8f) shows clear peaks between 196 and 204 eV, with binding energies at 196.9 and 200 eV attributed to $Cl2p_{3/2}$ and

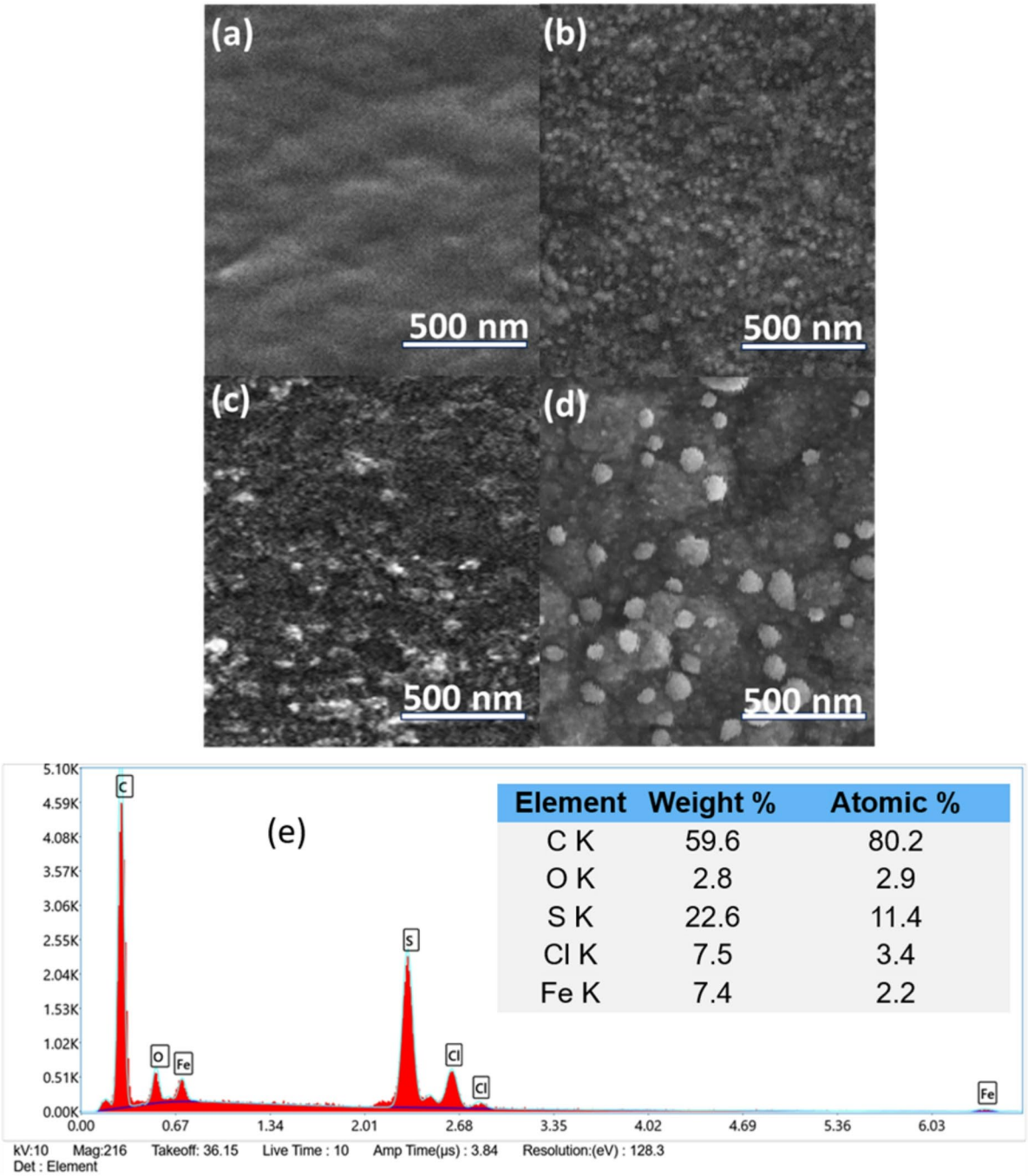

Fig. 5. FESEM images of undoped and $FeCl_3$-doped P3HT films: (**a**) P0 (undoped), (**b**) P20, (**c**) P40, (**d**) P60, and (**e**) EDX spectra.

$Cl2p_{1/2}$ of ionic Cl^-, confirming its presence within the P3HT matrix[36]. These Cl^- ions serve as counterions to maintain charge neutrality and stabilize the doped states. Overall, the XPS analysis confirms several key features of doping: oxidation of the P3HT backbone (evidenced by shifts and broadening in C1s and S2p), the incorporation of iron species with multiple oxidation states, and the presence of chlorine counterions. These spectral changes are consistent with the formation of delocalized charge carriers, supporting the enhanced electrical conductivity observed in $FeCl_3$-doped films. To further quantify the dopant incorporation, atomic percentage of the constituent elements were extracted from the survey spectra. The results are summarized in Table 2. The doped film P40 clearly shows the presence of Fe and Cl, with a higher Cl content relative to Fe, confirming the intercalation of Cl^- counterions that stabilize the doped states.

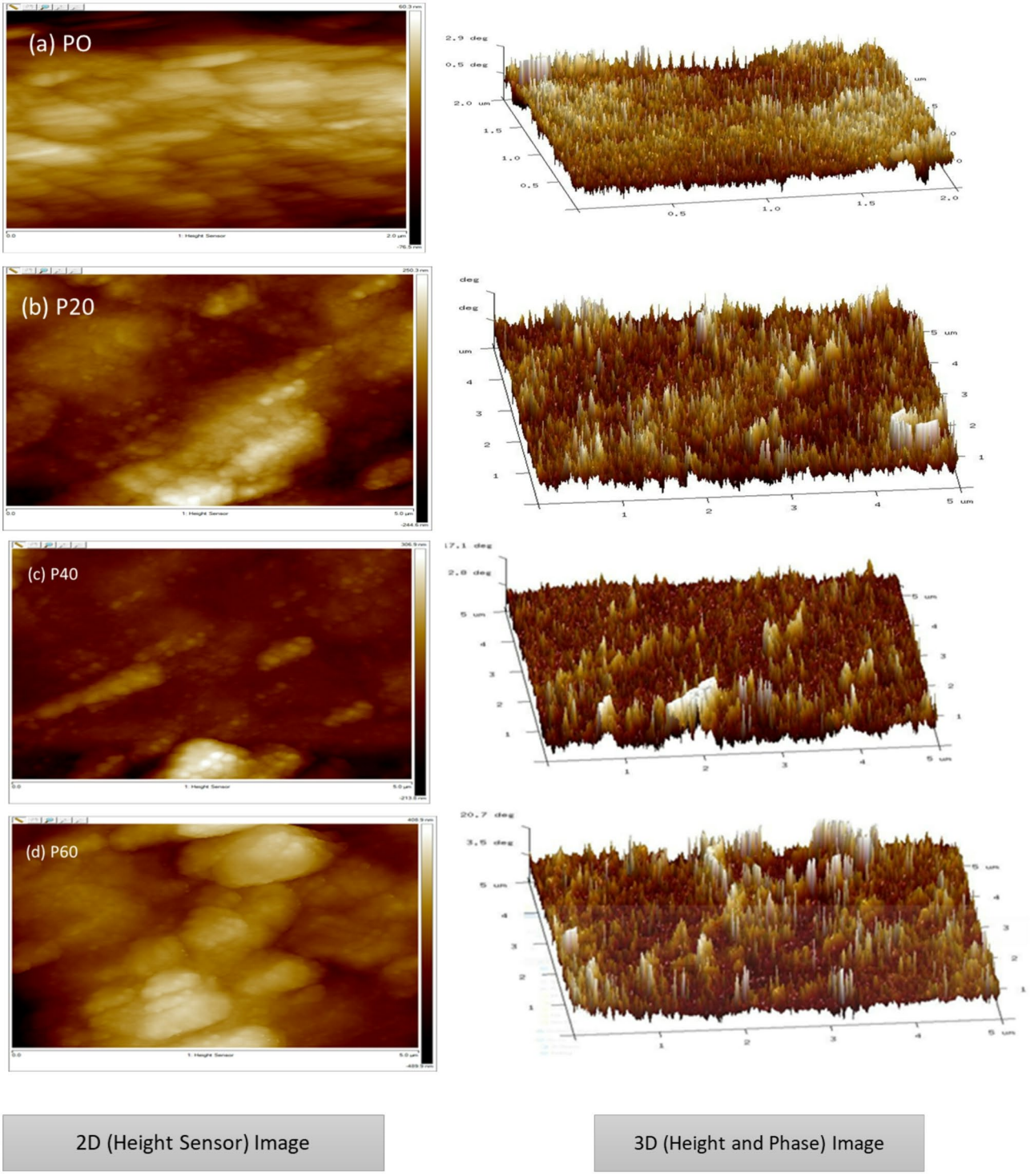

Fig. 6. AFM images (5 μm × 5 μm) of undoped and $FeCl_3$-doped P3HT films: (**a**) P0 (undoped), (**b**) P20, (**c**) P40, and (**d**) P60.

Thermoelectric measurements (Seebeck coefficient and resistivity)

The thermoelectric performance of materials is primarily governed by two parameters: the Seebeck coefficient (S) and electrical conductivity (σ), both of which critically influence the figure of merit (ZT). A high electrical conductivity is essential not only for improving ZT but also indicates low internal resistance, which enhances the material's efficiency as a thermoelectric voltage source. Conversely, the Seebeck coefficient represents the voltage generated per unit temperature gradient; a higher value of S implies a greater voltage output under the same thermal differential.

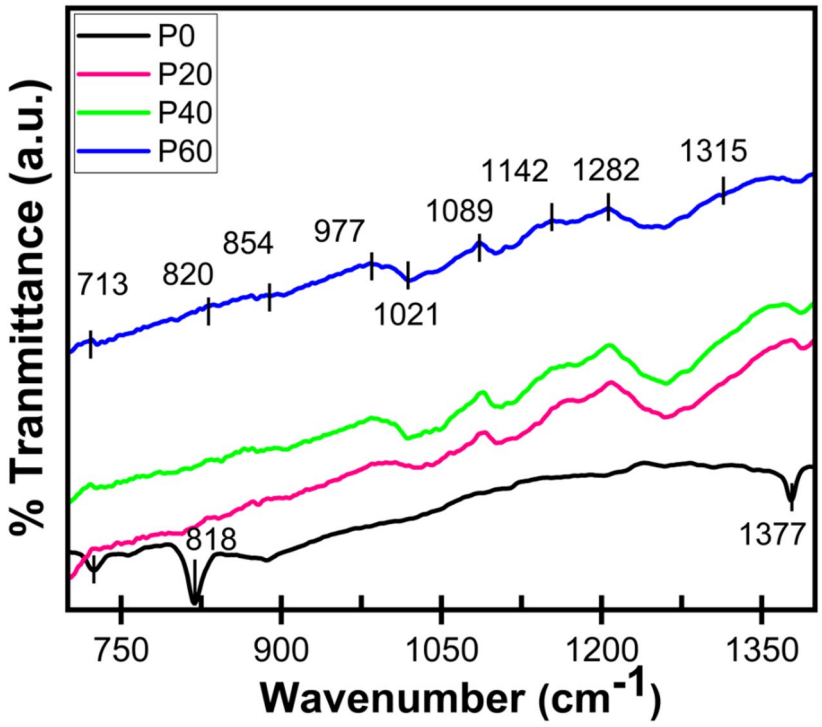

Fig. 7. FTIR spectra of undoped (P0) and $FeCl_3$-doped P3HT films (P20, P40, and P60).

To assess the combined influence of S and σ, the power factor (PF), defined as σS^2, is widely used. It serves as a comprehensive metric for evaluating energy conversion efficiency.

Figure 9(a) presents the variation in electrical conductivity for the undoped (P0) and $FeCl_3$-doped P3HT films (P20, P40, and P60) across different temperatures. The undoped P0 sample exhibited a low room-temperature (RT) conductivity of 4.37×10^{-4} S/cm, with a gradual increase upon heating. $FeCl_3$ doping led to a significant enhancement in σ, reaching 2.2 S/cm, 46.67 S/cm, and 13.7 S/cm at RT for P20, P40, and P60, respectively—an increase of more than four orders of magnitude compared to the undoped film. However, further increasing the doping concentration to 60 mM (P60) did not improve the conductivity beyond that of P40. Interestingly, the P60 sample displayed a pronounced temperature dependence, with σ increasing from 13.7 S/cm at 300 K to 69.8 S/cm at 400 K. This anomalous behavior suggests complex carrier dynamics at higher doping levels and merits further investigation. In contrast, P20 and P40 films showed only a weak dependence on temperature.

Turning to Seebeck coefficient measurements, Fig. 9(b) shows that the undoped film (P0) exhibited a modest S value of 25 μV/K at RT, indicative of its p-type nature. Doping with $FeCl_3$ significantly increased the Seebeck coefficient, with values of 112.7 μV/K, 164.9 μV/K, and 128.9 μV/K for P20, P40, and P60, respectively. These values are relatively high for conductive polymers and suggest strong p-type behavior dominated by positive ion transport. Notably, the P40 sample reached the highest S value of 164.9 μV/K at RT, which further increased to 181.1 μV/K at 400 K.

In comparison, PEDOT films treated with a superacid in methanol showed a dramatic increase in conductivity (from 0.7 to 2980 S/cm) but only a marginal improvement in S (from 17.6 to 21.9 μV/K)[37], underscoring the superior performance of $FeCl_3$-doped P3HT.

The enhanced S in doped samples can be attributed to both electronic and ionic contributions. Studies have shown that $FeCl_3$ introduces ionized species such as $(Fe_2Cl_5)^+$ and $(Fe_2Cl_7)^-$, in equilibrium with Fe_2Cl_6 dimers[34]. The hopping of Cl^- ions from these species contributes to ionic conduction in addition to the hole conduction resulting from $FeCl_3$-induced oxidation of the P3HT backbone. The doping process forms polarons and bipolarons, which serve as mobile positive charge carriers along the conjugated chains. However, at higher doping levels such as in P60, the increased concentration of Cl^- ions may lead to local ionic clustering, field perturbations, and dynamic disorder that impede hole transport[38].

The combined effect of enhanced conductivity and Seebeck coefficient is reflected in the power factor data shown in Fig. 9c. The P40 sample exhibited the highest PF of 127.4 $\mu W/mK^2$ at RT, which further increased to 178.5 $\mu W/mK^2$ at 400 K, demonstrating its superior thermoelectric performance among the studied films.

Discussion

The systematic investigation of undoped (P0) and $FeCl_3$-doped P3HT (P20, P40, and P60) films offers a comprehensive understanding of how chemical doping modulates the structural, morphological, and thermoelectric (TE) properties of P3HT, shedding light on its potential for thermoelectric applications. The XRD patterns of the undoped P3HT (P0) film revealed sharp, well-defined peaks indicative of a highly crystalline structure. These reflections correspond to specific crystallographic planes and are characteristic of

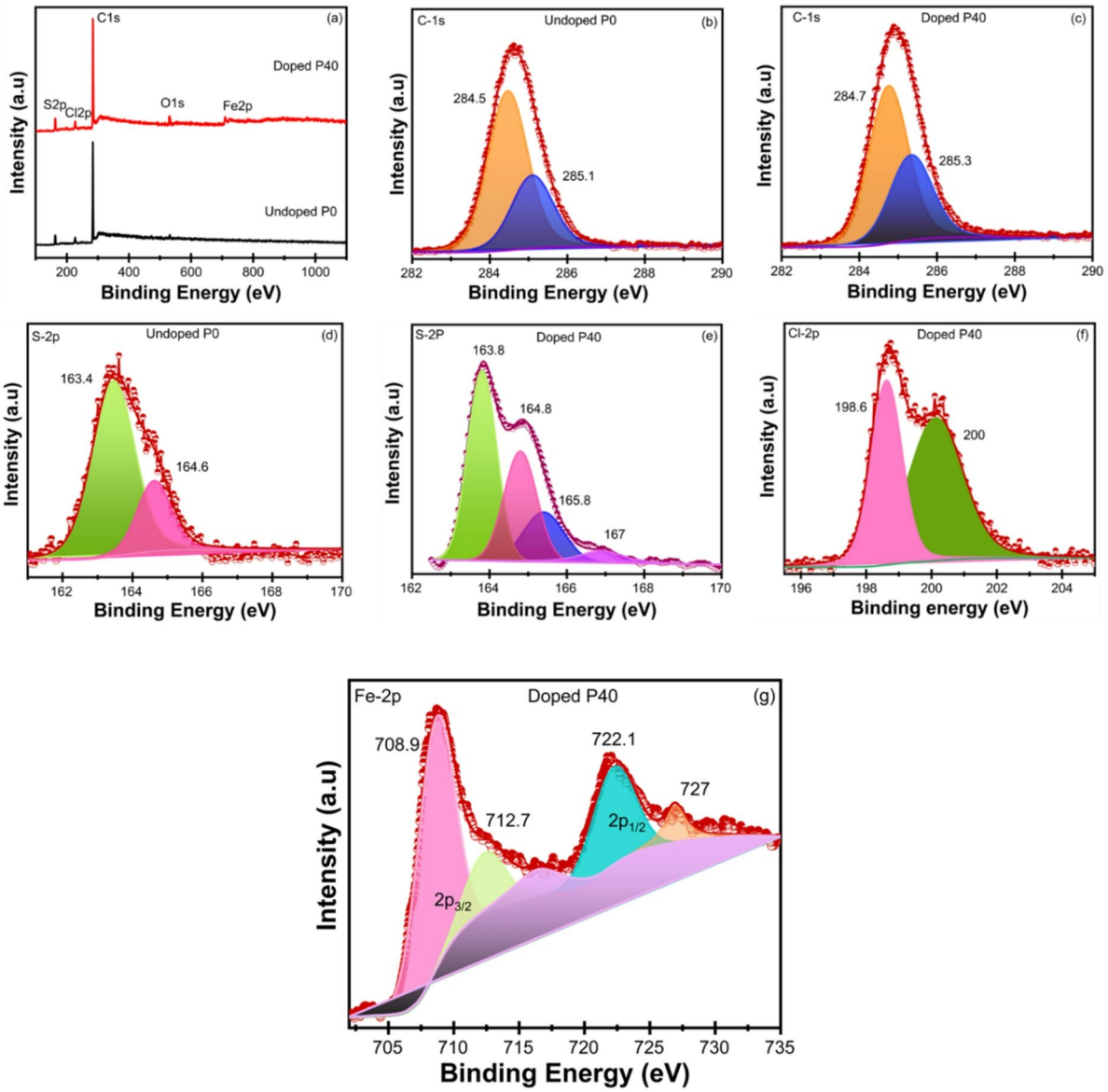

Fig. 8. XPS binding energy spectra of undoped (P0) and $FeCl_3$-doped P3HT film (P40): (**a**) wide scan; (**b**,**c**) C1s; (**d**,**e**) S2p; (**f**) Cl2p; (**g**) Fe2p.

Sample	C (at%)	S (at%)	O (at%)	Fe (at%)	Cl (at%)
P0 (Undoped)	72.1	16.8	11.1	–	–
P40 (Doped)	64.3	14.5	10.9	3.8	6.5

Table 2. Atomic concentration (at%) obtained from XPS spectra for undoped (P0) and $FeCl_3$- doped (P40) P_3HT films.

edge-on stacking, stabilized by strong π–π interactions among the aromatic rings. Upon doping with $FeCl_3$, the diffraction peaks not only reduced in intensity but also shifted toward lower angles, suggesting an increase in interplanar spacing due to ion intercalation. This broadening and shifting point to a loss of structural order and disruption of the crystalline domains, consistent with the formation of a more amorphous phase in the doped films.

Raman spectroscopy further corroborated these structural changes. A noticeable blue shift of the Cα = Cβ stretching mode from 1440 cm^{-1} in the undoped film to higher frequencies in the doped samples indicates a transformation in the polymer backbone, likely due to the formation of bipolarons. This shift is directly

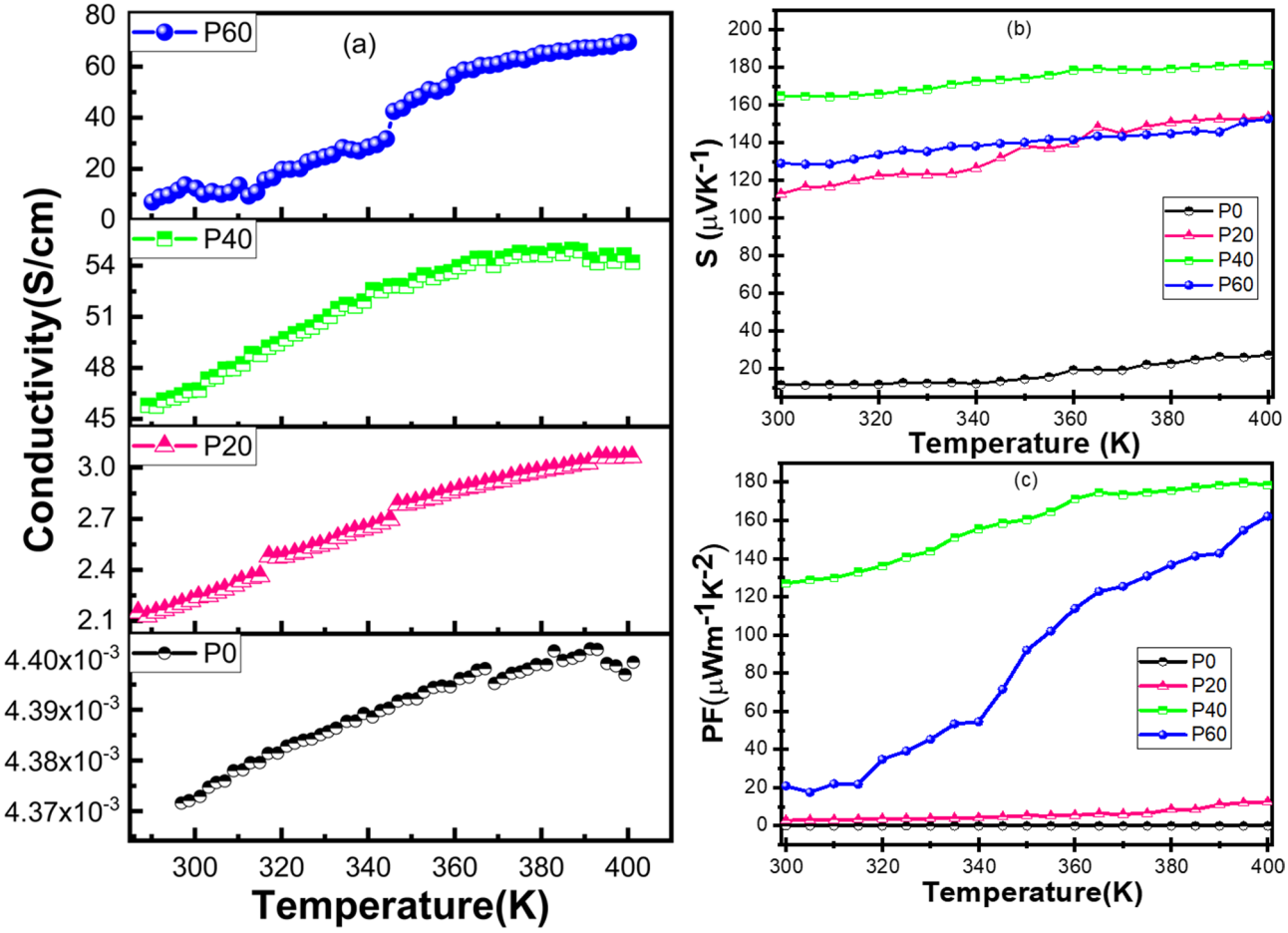

Fig. 9. (**a**) Electrical conductivity, (**b**) Seebeck coefficient, and (**c**) power factor for undoped (P0) and $FeCl_3$-doped (P20, P40, and P60) P3HT films.

associated with an increase in electrical conductivity. These structural modifications were also reflected in the film surface morphology.

FESEM and AFM analyses showed that the undoped films had a smoother surface with relatively small and uniform granules. The roughness (Rq) of the undoped sample was approximately 42 nm over a 5×5 μm^2 area. Doping with $FeCl_3$ resulted in a progressive increase in surface roughness and grain size, indicating localised polymer chain distortion and dopant clustering. Notably, higher doping concentrations (P60) led to a more heterogeneous and rough surface, which may affect the charge transport pathways. The EDX spectra confirmed the incorporation of Fe and Cl into the P3HT matrix, validating the successful doping and interaction between $FeCl_3$ and the polymer chains. The structural and morphological findings were further supported by FTIR and XPS analyses. FTIR spectra of the doped films showed the appearance of new peaks attributed to polaronic and bipolaronic states, particularly the intense 1142 cm^{-1} band, which is associated with delocalized positive charges along the polymer backbone. This suggests that bipolarons are the dominant charge carriers introduced by $FeCl_3$ doping. XPS provided additional evidence of chemical modification. In the doped films, new peaks corresponding to Fe2p and significant shifts in the C1s and S2p spectra were observed. These shifts confirm the oxidation of the thiophene ring and incorporation of $FeCl_3$, which introduces ionic species such as $(Fe_2Cl_7)^-$ and Cl^-. These ions not only contribute to the p-type conductivity by generating polarons and bipolarons but also play a role in ionic conduction.

The electrical conductivity and Seebeck coefficient of the films exhibited significant improvements with doping. The undoped P3HT film displayed a low conductivity of 4.37×10^{-4} S/cm and a Seebeck coefficient of 25 μV/K at room temperature. With $FeCl_3$ doping, electrical conductivity increased by more than four orders of magnitude, reaching a maximum of 46.67 S/cm for the P40 sample. Simultaneously, the Seebeck coefficient also improved significantly, achieving a maximum value of 164.9 μV/K at room temperature for the same sample. This concurrent enhancement in both σ and S is uncommon in thermoelectric materials and highlights the influence of ionic species and dopant-induced structural rearrangements in P3HT. The power factor (PF), a key parameter for evaluating TE performance, peaked at 127.4 $\mu W/mK^2$ at room temperature and further increased to 178.5 $\mu W/mK^2$ at 400 K for the P40 film. This performance makes P40 the optimal doping concentration, balancing structural order and charge carrier density to achieve superior thermoelectric efficiency. Interestingly, in the P60 films, both σ and S were lower than in P40 despite higher dopant concentration. This suggests that

Material/system	σ (S/cm)	S (μV/K)	PF (μW/mK²)	Temperature	References
$FeCl_3$-doped P3HT (This work, P40)	46.67	165.0	127.4	RT	This work
PEDOT: PSS (DMSO-treated)	~ 1000	~ 20	~ 4	RT	[40]
P3HT doped with CNT	~579	~ 29	~ 49	RT	[41]
P3HT/$TFSI^-$	~ 80	~ 50	~ 20	RT	[42]
CNT/P_3HT	~ 88	~ 11	~ 101	RT	[43]

Table 3. Comparison of thermoelectric performance of $FeCl_3$-doped P3HT with similar doped organic TE materials.

over-doping disrupts the polymer matrix beyond an optimal threshold, likely causing phase segregation, dopant aggregation, and morphological disorder. These phenomena hinder effective charge transport by introducing trap sites and breaking π–π stacking. As evidenced by FESEM and AFM, P60 exhibits pronounced surface roughness and heterogeneity, consistent with disrupted chain packing. The reduced mobility of charge carriers at this level of doping is also reflected in the strong temperature dependence of conductivity, pointing toward a thermally activated hopping mechanism common in disordered or over-doped conjugated polymers. Similar trends have been observed in other doped polymer systems, such as $FeCl_3$- and F4TCNQ-doped P3HT and PEDOT: PSS films[39], where excessive doping results in performance degradation due to structural over-disruption. This study highlights the remarkable potential of $FeCl_3$-doped P3HT for thermoelectric applications. Among the investigated samples, P40 emerges as the optimal composition, offering the best trade-off between microstructural order, carrier concentration, and TE performance. The thermoelectric properties of P3HT films with other dopants are summarized in Table 3.

Conclusion

In $FeCl_3$-doped P3HT films, the consistently positive Seebeck coefficient across all doping levels confirms that holes are the dominant charge carriers, consistent with effective p-type doping. Although ionic contributions—such as Cl^- mobility—may influence conductivity or introduce dynamic effects at higher doping concentrations, their role appears secondary to the primary hole-driven transport mechanism. This study demonstrates a viable strategy for enhancing the Seebeck coefficient (S) and power factor (PF) of P3HT through controlled chemical doping with $FeCl_3$. Among the tested samples, the P40-doped film showed the most balanced and enhanced thermoelectric performance, achieving an S of 164.9 μV/K and an electrical conductivity of 46.67 S/cm, resulting in a power factor of 127.4 $\mu W/mK^2$ at room temperature. This represents a significant improvement over the undoped P0 film, which exhibited a negligible PF of just 5.89×10^{-5} $\mu W/mK^2$. The results underscore the potential of tailoring organic-inorganic interactions in polymer nanocomposites to improve charge transport and thermoelectric performance. The observed enhancement in PF through strategic $FeCl_3$ doping highlights its effectiveness as a dopant for boosting the efficiency and stability of p-type conducting polymers like P3HT. Furthermore, the scalability, flexibility, and solution processability of these doped films make them promising candidates for large-area and low-cost thermoelectric devices. This study encourages further exploration of dopant–polymer interactions and offers a foundation for future investigations into solution-processable organic semiconductors for thermoelectric energy harvesting. Both neutral molecular design and dopant engineering approaches should be pursued to fully unlock the potential of polymer-based thermoelectrics.

Data availability

The datasets used and/or analyzed during the current study are available from the corresponding author on reasonable request.

Received: 19 March 2025; Accepted: 1 October 2025
Published online: 13 March 2026

References

1. Mori, T. & Priya, S. Materials for energy harvesting: at the forefront of a new wave. *MRS Bull.* **43** (3), 176–180 (2018).
2. Soleimani, Z., Zoras, S., Ceranic, B., Shahzad, S. & Cui, Y. A review on recent developments of thermoelectric materials for room-temperature applications. *Sustain. Energy Technol. Assess.* **37**, 100604 (2020).
3. Petsagkourakis, I. et al. Thermoelectric materials and applications for energy harvesting power generation. *Sci. Technol. Adv. Mater.* **19** (1), 836–862 (2018).
4. Nandihalli, N., Liu, C. J. & Mori, T. Polymer based thermoelectric nanocomposite materials and devices: fabrication and characteristics. *Nano Energy*. **78**, 105186 (2020).
5. Vashaee, D. & Shakouri, A. J. Improved thermoelectric power factor in metal-based superlattices. **92**(10), 106103 (2004).
6. Zhao, D., Fabiano, S., Berggren, M. & Crispin, X. Ionic thermoelectric gating organic transistors. *Nat. Commun.* **8**, 1 (2017).
7. Jiao, F. et al. Ionic thermoelectric paper. *J. Mater. Chem. A*. **5** (32), 16883–16888 (2017).
8. Choi, K., Kim, S. L., Yi, S., Hsu, J. H. & Yu, C. Promoting dual electronic and ionic transport in PEDOT by embedding carbon nanotubes for large thermoelectric responses. *ACS Appl. Mater. Interfaces*. **10** (28), 23891–23899 (2018).
9. Wang, H., Ail, U., Gabrielsson, R., Berggren, M. & Crispin, X. Ionic Seebeck effect in conducting polymers. *Adv. Energy Mater.* **5**(11) (2015).
10. Guan, X., Cheng, H. & Ouyang, J. Significant enhancement in the Seebeck coefficient and power factor of thermoelectric polymers by the Soret effect of polyelectrolytes. *J. Mater. Chem. A*. **6** (40), 19347–19352 (2018).

11. Zhao, D. et al. Polymer gels with tunable ionic Seebeck coefficient for ultra-sensitive printed thermopiles. *Nat. Commun.* **10**(1) (2019).
12. Wang, H. et al. Ionic thermoelectric figure of merit for charging of supercapacitors. *Adv. Electron. Mater.* **3** (4), 1700013 (2017).
13. He, M. et al. Thermopower enhancement in conducting polymer nanocomposites via carrier energy scattering at the organic–inorganic semiconductor interface. *Energy Environ. Sci.* **5** (8), 8351–8358 (2012).
14. Endrődi, B., Mellár, J., Gingl, Z., Visy, C. & Janáky, C. J. T. Molecular and supramolecular parameters dictating the thermoelectric performance of conducting Polymers: a case study using Poly (3-alkylthiophene) s. *J. Phys. Chem. C.* **119** (16), 8472–8479 (2015).
15. Xuan, Y. et al. Thermoelectric properties of conducting polymers: the case of poly(3-hexylthiophene). *Phys. Rev. B.* **82** (11), 115454 (2010).
16. Bounioux, C. et al. Thermoelectric composites of poly(3-hexylthiophene) and carbon nanotubes with a large power factor. *Energy Environ. Sci.* **6** (3), 918–925 (2013).
17. Rivnay, J. et al. Structural control of mixed ionic and electronic transport in conducting polymers. *Nat. Commun.* **7** (2016).
18. Endrődi, B., Mellár, J., Gingl, Z., Visy, C. & Janáky, C. Reasons behind the improved thermoelectric properties of poly(3-hexylthiophene) nanofiber networks. *RSC Adv.* **4** (98), 55328–55333 (2014).
19. Tokito, S., Smith, P. & Heeger, A. J. Highly conductive and stiff fibres of Poly(2,5-dimethoxy-p-phenylenevinylene) prepared from soluble precursor polymer. *Polymer* **32**, 464 (1991).
20. Zhang, Q., Sun, Y., Xu, W. & Zhu, D. Thermoelectric energy from flexible P3HT films doped with a ferric salt of triflimide anions. *Energy Environ. Sci.* **5** (11), 9639–9644 (2012).
21. Kumar, A., Patel, A., Singh, S., Kandasami, A. & Kanjilal, D. Apparatus for Seebeck coefficient measurement of wire, thin film, and bulk materials in the wide temperature range (80–650 K). *Rev. Sci. Instrum.* **90**(10) (2019).
22. Singh, R. K. et al. Structure–conductivity correlation in ferric chloride-doped poly(3-hexylthiophene). *New J. Phys.* **8** (7), 112 (2006).
23. Brinkmann, M. Structure and morphology control in thin films of regioregular poly(3-hexylthiophene). *J. Polym. Sci., Part B: Polym. Phys.* **49** (17), 1218–1233 (2011).
24. Yang, C. Y., Soci, C., Moses, D. & Heeger, A. J. Aligned rrP3HT film: structural order and transport properties. *Synth. Met.* **155** (3), 639–642 (2005).
25. Yamamoto, J. & Furukawa, Y. Electronic and vibrational spectra of positive polarons and bipolarons in regioregular Poly(3-hexylthiophene) doped with ferric chloride. *J. Phys. Chem. B.* **119** (13), 4788–4794 (2015).
26. Singh, R. K. et al. Micromorphology, photophysical and electrical properties of pristine and ferric chloride doped poly(3-hexylthiophene) films. *Mater. Chem. Phys.* **104** (2), 390–396 (2007).
27. Anthopoulos, T. D. et al. Air-stable complementary-like circuits based on organic ambipolar transistors. *Adv. Mater.* **18** (14), 1900–(2006).
28. De Leeuw, D., Simenon, M., Brown, A. & Einerhand, R. J. S. M. Stability of n-type doped conducting polymers and consequences for polymeric microelectronic devices. *Synth. Met.* **87** (1), 53–59 (1997).
29. Gregory, S. et al. Quantifying charge carrier localization in chemically doped semiconducting polymers. *Nat. Mater.* **20**, 1–8 (2021).
30. Singh, A. et al. Electrochemical investigation of free-standing polypyrrole–silver nanocomposite films: a substrate free electrode material for supercapacitors. *RSC Adv.* **3** (46), 24567–24575 (2013).
31. Wagner, C. D. J. Handbook of x-ray photoelectron spectroscopy: a reference book of standard data for use in x-ray photoelectron spectroscopy, (1979).
32. Beamson, G. J. I. High Relution XPS of Organic Polymers. The Scienta ESCA 300 Database, (1992).
33. Grosvenor, A. P., Kobe, B. A., Biesinger, M. C. & McIntyre, N. S. Investigation of multiplet splitting of Fe 2p XPS spectra and bonding in iron compounds. *Surf. Interface Anal.* **36** (12), 1564–1574 (2004).
34. Akdeniz, Z. & Tosia, M. P. Ionic conduction and molecular structure of molten FeCl3. *Z. für Naturforschung A.* **53** (12), 960–962 (1998).
35. Russo, M. et al. X-ray photoelectron spectroscopy and scanning Electron-microscopy characterization of novel Poly(monosubstituted)acetylenes containing doping species. *J. Vacuum Sci. Technol. a-Vacuum Surf. Films.* **16**, 35–44 (1998).
36. Yan, Z., Zhuxia, Z., Tianbao, L., Xuguang, L. & Bingshe, X. XPS and XRD study of FeCl3–graphite intercalation compounds prepared by Arc discharge in aqueous solution. *Spectrochim. Acta Part A Mol. Biomol. Spectrosc.* **70** (5), 1060–1064 (2008).
37. Wang, X. et al. Enhancement of thermoelectric performance of PEDOT: PSS films by post-treatment with a superacid. *RSC Adv.* **8** (33), 18334–18340 (2018).
38. Ahmed, A. A. & Salman *Development of milli-fluidic Device and Electronic Extrusion System for Fabrication of Sodium alginate/carbon Nanotube Microfibers* (Universiti Tun Hussein Onn, 2024).
39. Huang, W. & MacDiarmid, A. J. P. *Opt. Prop. Polyaniline*, **34**(9) 1833–1845. (1993).
40. Bubnova, O. et al. Optimization of the thermoelectric figure of merit in the conducting Polymer Poly (3, 4-ethylenedioxythiophene). *Nat. Mater.* **10** (6), 429–433 (2011).
41. Qu, S., Wang, M., Chen, Y., Yao, Q. & Chen, L. J. Enhanced thermoelectric performance of CNT/P3HT composites with low CNT content. *RSC Adv.* **8** (59), 33855–33863 (2018).
42. Zhang, Q., Sun, Y., Xu, W. & Zhu, D. J. E. Thermoelectric energy from flexible P3HT films doped with a ferric salt of triflimide anions. *Energy Environ. Sci.* **5** (11), 9639–9644 (2012).
43. Hong, C. T., Kang, Y. H., Ryu, J., Cho, S. Y. & Jang, K. S. Spray-printed CNT/P3HT organic thermoelectric films and power generators. *J. Mater. Chem. A.* **3** (43), 21428–21433 (2015).

Acknowledgements

VR would like to acknowledge UPES, Dehradun for providing fellowship and research facilities. AK would also like to acknowledge the funding received from SERB, India, through the SRS scheme.

Author contributions

Vaishali Rathi: Material synthesis, investigation, conceptualization, methodology, visualization, data curation, formal analysis, writing original draft. Manoj Sathwane: data curation, formal analysis, review and editing original draft. Kamal Singh: editing manuscript. Pradip K. Maji: manuscript review and editing. K.P.S. Parmar: supervision, manuscript editing and review. Ranjeet K. Brajpuriya: resources, supervision, manuscript editing and review. Ashish Kumar: resources, manuscript editing and review, supervision, funding acquisition.

Declarations

Competing interests

The authors declare no competing interests.

Additional information

Correspondence and requests for materials should be addressed to V.R., R.K.B. or A.K.